Scanning surface plasmon imaging of nanoparticles

T. Roland,[1,2] L. Berguiga,[1,2] J. Elezgaray,[3] and F. Argoul[1,2]
[1]*Université de Lyon, F-69000 Lyon, France*
[2]*USR 3010 and UMR 5672, CNRS, Ecole Normale Supérieure de Lyon, 46 Allée d'Italie, F-69007 Lyon, France*
[3]*UMR 5248, ENITAB, CNRS–Université Bordeaux 1, 2 rue Robert Escarpit, F-33607 Pessac, France*
(Received 21 May 2010; published 11 June 2010)

Confining surface plasmon resonance with a high-resolution heterodyne interferometric microscope, we demonstrate that subwavelength nanoparticles (10–200 nm in diameter) can be identified and sized in air and water media. Even though this microscope does not require any labeling of the nanoparticles, it offers the possibility to distinguish metal from polymer nanoparticles, by the identification of an angular transform of the backreflected field $[V(Z)]$ versus the defocus Z. We propose a simple model that reproduces the optical response of the microscope in the presence of a nanoparticle perturbation. Both the shape of the microscope point spread function and the $V(Z)$ curves compare well with the experimental data, confirming the possibility to discriminate metal from polymer nanoobjects with this microscope.

DOI: 10.1103/PhysRevB.81.235419 PACS number(s): 73.20.Mf, 03.50.De, 78.67.Bf

I. INTRODUCTION

Surface plasmon resonance (SPR) is a collective response of free-surface electrons of conducting materials to an electromagnetic excitation.[1] The field enhancement associated with SPR makes it suitable for high sensitivity detection of nanoscale objects.[2] When SPR is launched on a flat metal surface, it propagates and attenuates on a characteristic distance ℓ_x^{SP} which is on the order of several micrometer. Localized surface plasmon polaritons (SPPs) were first obtained by light absorption by metal nanoparticles (NPs) (Ref. 3) and later on textured metal films.[4] SPP confinement can also be achieved using a high numerical aperture objective lens.[5–8] Scanning surface plasmon microscopy (SSPM), based on this method, was shown to improve the resolution of SPR imaging by more than one order of magnitude.[5–7]

Optical properties of NPs are intermediate between bulk material and molecular aggregates, they depend not only on their size but also on their shape.[9] Both near-field[10] and far-field[11] optical detection of nanoparticles have been proposed so far. Since the intensity of light scattered by a NP scales as D^6 (D being the particle diameter), the discrimination of a single particle from other scatterers requires long integration times. Interferometric methods pushed down this size limitation by capturing the field scattered by the particle ($\sim D^3$). Recently, photothermal heterodyne imaging was proposed for detecting gold NPs with diameters as small as 1.4 nm with an integration time of a few milliseconds.[12] Imaging low-index dielectric particles is mainly limited by the contrast difference with the surrounding medium. Very few studies afford the detection of unlabeled particles with sizes much smaller than the wavelength. Recently, Ignatovich and Novotny[13] have proposed an interferometric device that pushes the detection limit down to 20 nm diameter for polymer particles within a few milliseconds.

We show that SSPM can be used to image NPs of different materials (metal, dielectric) for diameters ranging from 10 to 200 nm in air and water. This is, to our knowledge, the first evidence for a single technique which can offer a fast, direct, versatile, and nonintrusive imaging of nanosize objects. We also discuss the SSPM contrast optimization with a mean-field multilayer model, and we confirm that the particle contrast oscillations with the microscope focus Z depends mainly on the phase of the backreflected field reradiating through the objective lens.

II. MATERIALS AND METHODS

A. SSPM setup

Figure 1(c) reports the sketch of the SSPM optical setup.[6] A linearly polarized He-Ne ($\lambda = 632.8$ nm) laser beam is collimated, expanded 15 times and finally focused on the sample by an immersion objective lens with a large numerical aperture 1.45 NA 60× (respectively, 1.65 NA 100×) for air (respectively, water) observation. An heterodyne interfer-

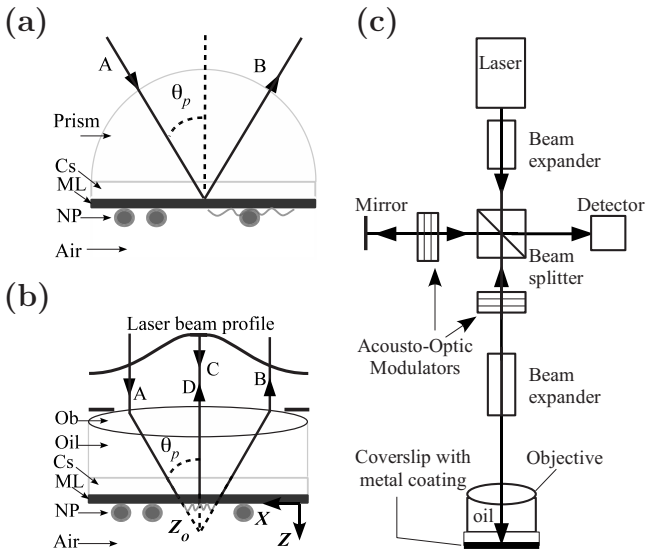

FIG. 1. (a) Prism-coupled Kretschmann configuration for SPR measurements. (b) High numerical aperture lens-coupled SPR imaging system. (c) Sketch of the SSPM apparatus. (A,C) incoming and (B,D) backreflected rays, Ob: objective lens, Cs: coverslip, ML: metal layer, NP: nanoparticle, and θ_p: SPR angle.

ometer enables the detection of phase differences (between reference and sample arms) introduced by SPR [Fig. 1(a)]. Disposable microscope coverslips coated with a 3 nm layer of chromium and a ~45 nm layer of gold serve as surface plasmon resonators. A 500×500 pixel SSPM image $I(X,Y)$ is recorded in a few seconds by scanning the sample with a $(X\text{-}Y)$ piezoelectric stage [PI FRANCE] at a fixed defocus Z. To get rid of laser intensity fluctuations, for each point (X,Y), the signal I is normalized by the maximal value I_0 of $I(Z)$ at $(X,Y)=(0,0)$. The Z defocus value corresponding to this maximal value I_0 is then chosen as the origin $Z=0$. This position corresponds roughly to the gold/dielectric medium interface. At focus ($Z=0$) and out of focus ($Z>0$), incoming rays (A) are reradiated in rays (B), containing amplitude and phase information on SPP propagation inside the confined area [see Fig. 1(b)]. The radial symmetry of the high-aperture objective lens produces a confinement of the SP waves. The rays (C) which are not coupled to SP are reflected back (D) without SP phase retardation.

B. Sample preparation

Deposition of NPs on gold surface was optimized to have isolated objects. The gold samples were first rinsed with absolute ethanol, dried under a nitrogen flow, and cleaned by O_3, in a UV/O_3 chamber (45 min). All calibrated (C) and noncalibrated (NC) gold NPs were dispersed in ultrapure water (18 $M\Omega$ cm^{-1}) to a final concentration of $\sim10^8$ ml^{-1}. A drop of this dispersion (~300 μl) was deposited on gold (2 min), rinsed with 3 ml of ultrapure water, and dried under a nitrogen flow. Latex NP adsorption was favored by self-assembling a monolayer of 11-Amino-1-undecanethiol (AUT) molecules on gold. C and NC latex particles were dispersed to a final concentration of $\sim10^7$ ml^{-1} in a phosphate buffer (pH=8 and 100 mM ionic strength). A drop of 300 μl of this solution was deposited onto the AUT-SAM (self-assembled monolayer) gold surface and stored 20 h in an air oven at 80 °C. The samples were rinsed with 1 ml of ultrapure water and dried under nitrogen gas before SSPM imaging. Atomic force microscopy was performed to check the sparse concentration of gold and latex NPs on the gold surface ($\sim1/\mu m^2$). Both gold and latex NPs adsorbed on gold were first localized and imaged with SSPM in air, then the microflow chamber in contact with gold was filled with water to allow water medium observation.

III. SPR VERSUS SSPM PRINCIPLES

Surface plasmon excitation can be achieved by monitoring the wave-vector component normal to the gold interface in attenuated total reflection, thanks to a prism coupler, for instance, with the Kretschmann[14] or the Otto geometry.[15] In the Kretschmann geometry, a prism with refractive index n_g is covered by a metal waveguide consisting of a thin metal film (with permittivity $\varepsilon_m=\varepsilon'_m+i\varepsilon''_m$) and thickness δ_m, in contact with a semi-infinite dielectric medium (ε_D). The reflectivity curves shown in Figs. 2(a) and 2(b) have been computed using Fresnel refraction and reflexion equations and a four-layer model for the metal interface

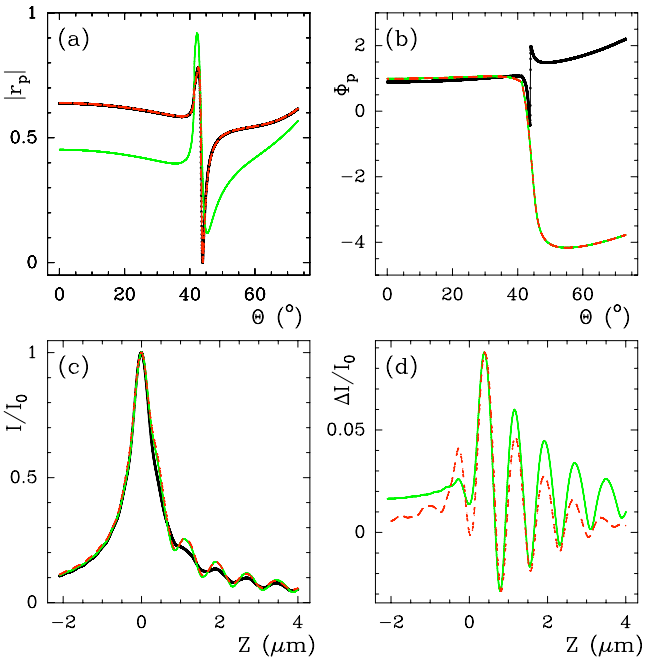

FIG. 2. (Color online) (a) SPR reflectivity $|r_p(\theta)|$ curves (black symbols for a 45-nm-thick gold film and green curve for a 25-nm-thick gold film). (b) Phase of r_p: Φ_P [black symbols correspond to a 45-nm-thick gold film, light gray (green in color) and dark gray (red in color) curves correspond to a 25-nm-thick gold film]. (c) I/I_0 curves (normalized to their maximum). The dark gray (red in color) curve corresponds to an artificial layer with the $|r_P|$ of a 45-nm-thick gold film and the Φ_P of a 25-nm-thick gold film. (d) Contrast versus Z plots, computed from the differences of the dark gray (red in color) and light gray (green in color) curves $I/I_0(Z)$ with the black $I/I_0(Z)$.

(glass/chromium/gold/air).[16,17] The propagation constant (k_x^{SP}) for surface plasmon in a Kretschmann configuration can be written as[18]

$$k_x^{SP}=k_x^{SP\infty}+\Delta k_x^{SP}=\frac{\omega}{c}\sqrt{\frac{\varepsilon_D\varepsilon_m}{\varepsilon_D+\varepsilon_m}}+\Delta k_x^{SP}. \quad (1)$$

The first term characterizes the surface plasmon propagation at a two semi-infinite medium (metal-dielectric) interface without prism, and Δk_x^{SP} accounts for the prism coupling, that produces the evanescent wave and the finite size of the gold film.[19] The attenuation length of the surface plasmon waves $\ell_x^{SP}=1/[2\Im(k_x^{SP})]$ depends on the thickness of gold and on its texture (volume and surface). When the thickness of gold is decreased from 45 to 25 nm, radiative damping[20] increases and this propagation length is roughly divided by 2, which produces a weak localization of the surface plasmon.

A. One-dimensional modeling of $I(Z)$ curves

When the objective lens is scanned along the Z axis, a complex $V(Z)$ signal is recorded on the photomultiplier. This signal $V(Z)$ is at the basis of SSPM image reconstruction. It can be written as an average of the black reflected field over the incident rays characterized by the two angles θ and φ,[5]

$$V(Z) = \int_{\theta_{\min}}^{\theta_{\max}} P^2(\theta)\mathcal{Q}(\theta)\exp(2jk_g Z\cos\theta)\sin\theta d\theta, \quad (2)$$

where P is the pupil function of the objective lens, k_g the wave number inside glass, $\mathcal{Q}(\theta)$ is proportional to the back-reflected field, integrated over the radial angle φ and it depends on the light polarization (P for TM polarization and S for TE polarization), in the case of a flat interface (no NP),

$$\mathcal{Q}^{P,S}(\theta) = \int_0^{2\pi} r^{P,S}(\theta)\cos^2\varphi d\varphi = \pi r^{P,S}(\theta). \quad (3)$$

B. Dependence of $V(Z)$ curves with the gold film characteristics

We concentrate here our discussion on the modulus $I(Z)$ of $V(Z)$ and we consider a linear polarization configuration. As shown in Fig. 2(c), a $I(Z)$ curve presents a sharp central peak aligned on $Z=0$, and for $Z>0$ (focusing inside the dielectric medium) smooth and slow oscillations, characteristic of plasmon resonance, that superimpose to a global decay. Their period can be approximated by the equation $\Delta Z_{SP} = \lambda/2n_g(1-\cos\theta_P)$ (Refs. 5 and 21) with θ_P the angle of plasmon resonance [$\simeq 44°$, as shown in Fig. 2(a)] which gives $\Delta Z_{SP} \sim 744$ nm.

C. SSPM and radiative damping

The interfacial reflectivity $r^P(\theta)$ is a complex quantity, and besides a deap hollow of $|r_P|$ at plasmon resonance, its phase $\Phi_P(\theta)$ also displays a sharp drop. When the thickness of the gold film changes, both the shape of $|r_P(\theta)|$ and the drop of the phase at resonance change dramatically [see Figs. 2(a) and 2(b)]. In Fig. 2, we use two gold thicknesses for illustration, respectively, 45 nm (black curve) and 25 nm (light gray curve, green in color) to demonstrate that the phase $\Phi_P(\theta)$ has a dominant role on the $I(Z)$ response. We construct an artificial "hybrid" film, with $|r_P|$ corresponding to a 45-nm-thick gold and Φ_P corresponding to a 25-nm-thick gold (red curves). The corresponding normalized $I/I_0(Z)$ curves are plotted in Fig. 2(c). Despite the $|r_P|$ of dark gray (red) (hybrid film) and black (45 nm film) curves are the same, the corresponding $I/I_0(Z)$ are very different. Actually, the hybrid film $I/I_0(Z)$ curve looks much more like the 25 nm film $I/I_0(Z)$ curve. In Fig. 2(d), we plot the difference between each of the dark gray (red) and light gray (green) curves and the black curve which corresponds to the 45-nm-thick gold film. We conclude from this figure that the $I(Z)$ slow-mode oscillations, characteristic of plasmon are more sensitive to the phase than to the amplitude of r_P. Decreasing the gold thickness δ_m involves an amplification of these oscillations. The shortness of the plasmon propagation length ℓ_x^{SP} due to radiative damping involves an improvement of the SSPM contrast.

D. Experimental curves

$I(Z)/I_0$ curves shown in Fig. 3(a) were acquired from a 45 nm gold layer deposited on a 3 nm chromium layer to ensure adhesion on glass. NPs were adsorbed on gold prior to the experiments. The gray curve with symbols corresponds to a point (X,Y) located on the bare gold surface while the gray curve without symbol corresponds to a 100 nm gold NP.

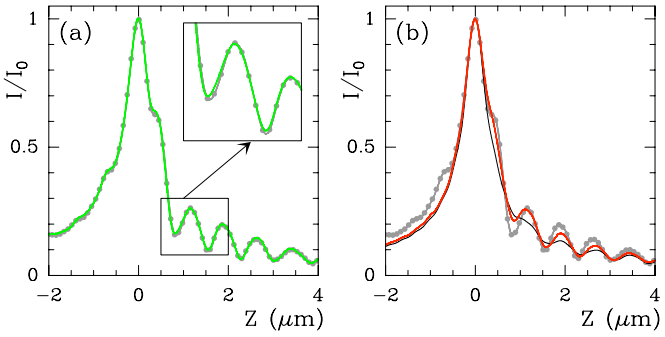

FIG. 3. (Color online) (a) Experimental $I/I_0(Z)$ curves, captured for a bare gold zone (gray curve with symbols) and for a position corresponding to an adsorbed NP (gray curve, green in color). (b) Modeling the experimental curve $I/I_0(Z)$ (gray curve with symbols) with the mean-field model: black curve computed for a 45 nm gold layer and red curve computed from a 45 nm gold layer, with a modification of the phase of the reflectivity Φ_P, to decrease the plasmon propagation length (for instance, for a gold layer thickness of 25 nm). Model parameters: $\varepsilon_1 = -12.0 + i1.2$ for gold, $\varepsilon_{chr} = -1.11 + i20.8$ for chromium (3 nm), pupil function $P(\sin\theta) = \exp(-2\sin^2\theta/w^2)$ with $w=0.8$.

With a Gaussian pupil function and including a chromium adhesive layer of 3 nm to gold, we computed $I/I_0(Z)$ curves that reproduce fairly well the shape of the experimental curves, as shown in Fig. 3(b). The 45 nm thickness of the gold films was confirmed by measurement of SPR $|r_P|$.[16,22] The computation of $I/I_0(Z)$ with a four-layer model (glass/3 nm chromium/45 nm gold/air) gives the black curve in Fig. 3(b), that does not fit the experimental curve. Therefore, SSPM experimental response cannot be fully interpreted on the basis of this model with a flat gold film. If we compare the experimental $I(Z)$ curves [Fig. 3(a)] with the theoretical curves of Fig. 2(c), we conclude that there must be some SP localization phenomenon in the experimental data. This SP localization suggests that the gold layers prepared by gold evaporation do not behave as flat and homogeneous layers and that their inhomogeneity (lacunarity and/or roughness) may change (shorten) the propagation length of the plasmon.[16,22] To take into account this inhomogeneity, we propose here to tune the phase of the reflectivity Φ_P. As suggested above, in Fig. 2, we have replaced the phase of r_P of a 45 nm gold layer, by the phase of a thinner gold layer (25 nm), and we plot the new $I/I_0(Z)$ profile in red. This theoretical curve gives a better prediction of the experimental data.

IV. SURFACE PLASMON AND GOLD ROUGHNESS

The localization of SP by rough surfaces was very early predicted by Raether.[1] Imaging naked gold film surface with SSPM can be used to reveal the spatial inhomogeneity of gold films. We have observed[16,22] a strong dependence of the SSPM response (amplitude and phase) with the roughness of

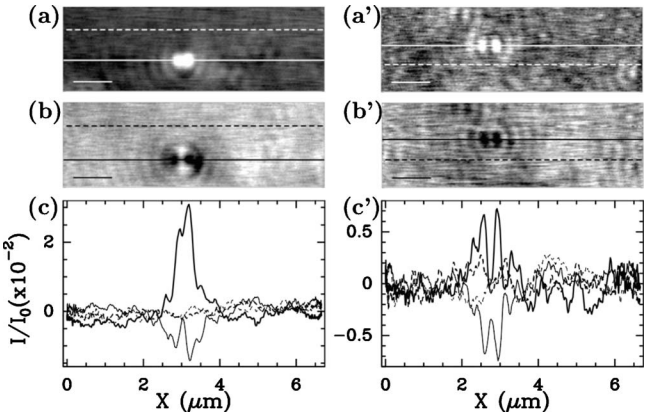

FIG. 4. SSPM images of NPs in air. Left panels: 200 nm gold NP. Gray-coded images constructed for $Z=0.825$ μm (a) and 1.150 μm (b). In (c) are shown sections of (a) and (b). Right panels: 50 nm gold NP. Gray-coded images constructed for (a′) $Z=0.925$ μm and (b′) 1.330 μm. In (c′) are shown sections of (a′) and (b′). White (respectively, black) section lines in (a) and (a′) [respectively, (b) and (b′)] correspond to thick (respectively, thin) curves in (c) and (c′). Scale bar is 1 μm.

gold. It produces an inhomogeneous distribution of the electric field at the gold interface. This roughness produces "hot spots" where the local electric field can be dramatically increased, and modifies the lateral propagation length $\ell_x = 1/(2k_x''^{\mathrm{SP}})$ of the surface plasmon. In other words, the larger the volume fraction of defects (due to its roughness) the shorter the lateral propagation length of the plasmon wave, in a similar way as thinner gold films (see Fig. 2).

V. NANOPARTICLE IMAGING WITH SSPM

Figure 4 shows SSPM images of gold and latex NPs in air. They were flattened using a second-order polynomial and filtered with a nine pixel sliding box. Averaged cross sections obtained from gold and latex NPs imaged in air, with size ranging from 10 to 200 nm, are shown in Fig. 5. Images of NPs were also obtained in water for latex and gold NPs with sizes ranging from 30 to 200 nm (see Fig. 6).

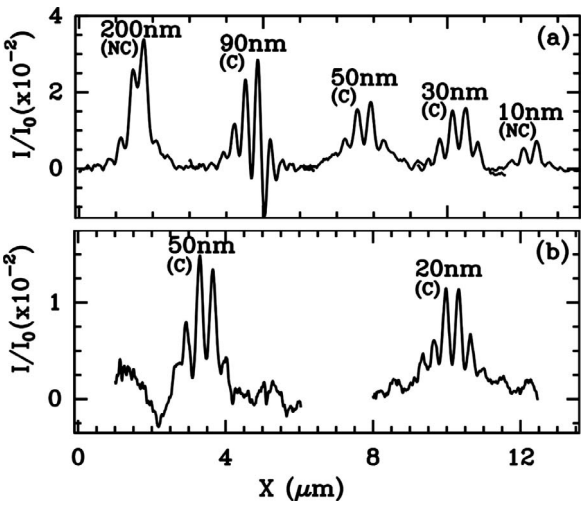

FIG. 5. Comparison of SSPM image cross sections of (a) gold and (b) latex NPs of different sizes. In (a), the 200 nm and 10 nm profiles have been averaged over 3 and 6 noncalibrated NPs, respectively, whereas the 90, 50, and 30 nm profiles have all been averaged over 4 calibrated NPs. In (b), the 50 nm and 20 nm NP profiles have been averaged over 2 and 6 calibrated NPs, respectively.

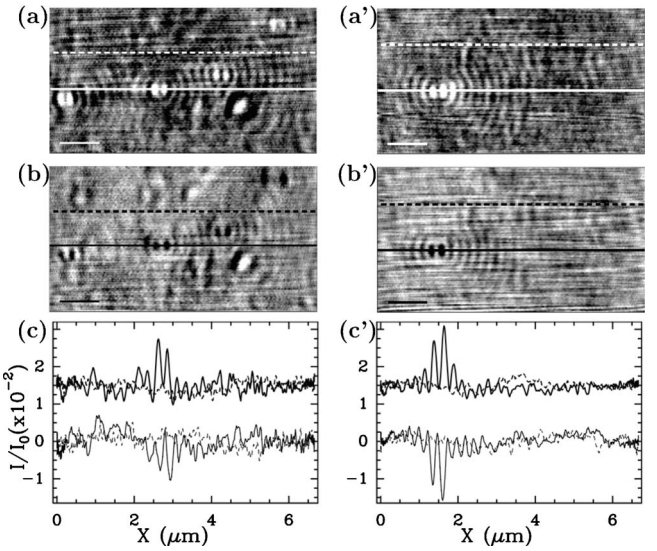

FIG. 6. SSPM images of calibrated NPs in water. Left panels: 30 nm gold NP. Gray-coded images constructed for (a) $Z=1.270$ μm and (b)1.100 μm. In (c) are shown some sections of (a) and (b). Right panels: 30 nm latex NP. Gray-coded images constructed for (a′) $Z=0.767$ μm and (b′) 0.500 μm. In (c′) are shown sections of (a′) and (b′). White (respectively, black) section lines in (a) and (a′) [respectively, (b) and (b′)] correspond to thick (respectively, thin) curves in (c) and (c′). Scale bar is 1 μm. Intensity profiles corresponding to positive contrast in (a) and (a′) have been artificially shifted upward in (c) and (c′).

With a linearly polarized light, NPs adsorbed on the gold surface appear as a two-lobe pattern in the direction of the P polarization.[7] The separation and the width of the two lobes do not depend on the size and the nature of the NP if smaller than the point spread function (PSF) width, which can be estimated from the full width at half maximum (FWHM) of each lobe: 220 ± 20 nm in air and 135 ± 20 nm in water. The corresponding mean distances between the two lobes are 350 ± 20 nm in air and 245 ± 15 nm in water. However, when the NP size reaches 200 nm, the two lobes are no longer separated and their intensities overlap [see Fig. 5(a)]. Going from air to water, the PSF width diminishes by a factor 2/3, with a weak dependence on the nature of the NP.

Thanks to the decomposition of Maxwell equations on a multipolar expansion,[23] we computed numerically the two-lobe characteristic SSPM response for a spherical 50 nm metal NP in air [Fig. 7(a)]. This profile is a J_1 Bessel function whose axis is parallel to the direction of the incident polarization. The theoretical cross section provides a remarkable fit of the experimental data, obtained from both gold and latex NPs [Fig. 7(b)]. The predictions of the PSF FWHM (240 nm in air and 150 nm in water) and of the distance of the lobes (340 nm in air and 255 nm in water) compare well with the experimental values. The contrast a NP with the

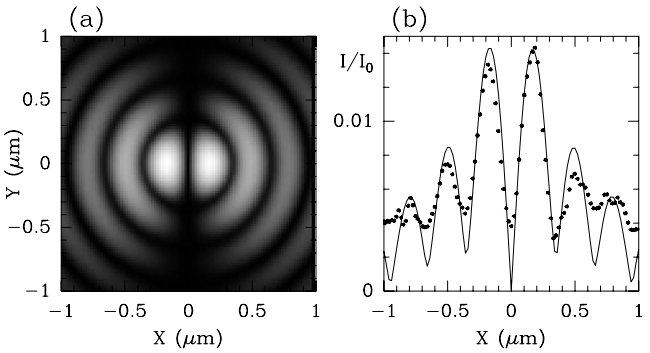

FIG. 7. (a) Theoretical gray-coded intensity $I(X,Y)/I_0$ computed for a 50 nm gold NP in air at $Z=800$ nm. (b) Cross section of (a) at $Y=0$ (solid line), compared to the corresponding experimental section (black dots). In the theoretical model, the particles are embedded in air and separated by 0.1 nm from the 45 nm gold layer ($\varepsilon_1 = -12.0+i1.2$) coated on a glass coverslip.

surrounding medium (ε_4) is approximated by the ratio $(\varepsilon_{\mathrm{NP}} - \varepsilon_4)/(\varepsilon_{\mathrm{NP}}+2\varepsilon_4)$, and for a latex particle, this ratio decreases from 0.34 (air) to 0.13 (water), which is in the opposite sense than what we observe with the SSPM. We interpret this difference by a strong widening of the reflectivity r_P curve in water, which improves the SSPM contrast.

However, the contrast of the NPs, given by the difference ΔI of the lobe maxima with the background, changes very slowly with their size and/or their nature. This experimental behavior can be explained by the fact that the gold film captures the nonradiative field backreflected by the particle which decreases slowly with the particle size since it is given by the particle polarizability. Close to the particle, a very strong-field gradient occurs, which interferes locally with the evanescent field of the gold film. Moreover, if the gold interface is rough there will be an amplification of the evanescent field due to SPR, and a localization of this field on hot spots.

We show now that the evolution of the optical contrast $\Delta I(Z)$ with the defocus Z can be used to differentiate the dielectric properties of two spherical particles. This information can be retrieved from the evolution of the optical response with the defocus. Related to the dielectric property of the NP, a phase shift of $\Delta I(Z)$ oscillations occurs, as shown in Fig. 8 for two sets of NPs, respectively, 100 nm gold in Fig. 8(a) and 100 nm latex in Fig. 8(b). For instance, the first minimum is at $Z=0.5$ μm for a 100 nm gold particle and at $Z=0.7$ μm for a 100 nm latex particle, which gives a shift ~ 200 nm. This is a robust phenomenon that reproduces independently of the size of the NP. We also compare the experimental contrast curves (gray curves with symbols) with the prediction of the four-layer model, computed either with a 45 nm gold layer (plain black curve), or the hybrid gold film, where the phase of the plasmon reflectivity corresponds to a 25 nm gold layer, to shorten the lateral propagation length [gray (red in color) dashed curve]. We note that the modification of the phase of the reflectivity changes the contrast curves versus Z and improves also the correspondence between theoretical and experimental curve.

Since we did not quantify yet the effect of inhomogeneity of gold layer on SPP propagation length, we have introduced this phenomenological model that takes into account in a

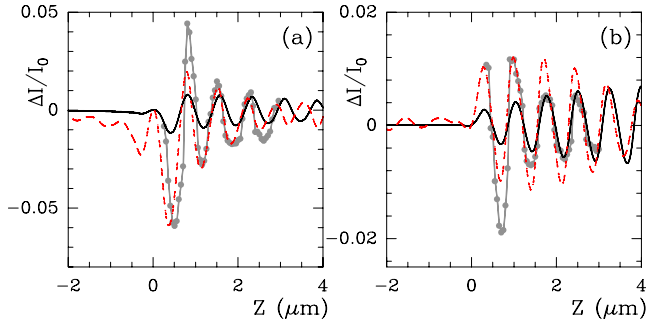

FIG. 8. (Color online) (a) Experimental SSPM contrast of a 100 nm gold particle (gray curve with symbols). Black and dashed gray curve (red in color): predictions of a four-layer model. The NP is replaced in this model by an extra 10 nm gold layer. (b) Experimental SSPM contrast of a 100 nm latex particle (gray curve with symbols). Black and dashed red curves: predictions of our four-layer model. The NP is considered in our model as an extra 5 nm latex layer. Model parameters: $\varepsilon_1 = -12.0+i1.2$ for gold, $\varepsilon_{chr} = -1.11 + i20.8$ for chromium (3 nm), pupil function $P(\theta) = \exp(-2\sin^2\theta/w^2)$ with $w=0.8$. The black curves correspond to a 45 nm gold layer and the red dashed curves correspond to an hybrid 45 nm gold layer whose reflectivity phase Φ_P is matched to a 25 nm gold layer (red dashed curve).

similar way the decrease in SPP propagation length. It reproduces well the phase differences in the behavior of the contrast $\Delta I(Z)$ against the defocus, both in amplitude and in position of the extrema. The result reported in Fig. 8 is original since it suggests that mixed metal and polymer NPs can be separated by SSPM. It can be justified by the fact that the function $\mathcal{Q}(\theta)$ describing the interfacial plasmon reflectivity changes with the real or complex value of the index of the medium in contact with gold.

VI. CONCLUSION

To summarize, we have shown that SSPM is a highly sensitive technique for detecting nanosize particles. The information about the size of the NP is mainly contained in the amplitude of the PSF of this microscope and its index characteristics can be enlightened from the $\Delta I(Z)/I_0$ curves. The good agreement between experiments and computations proves the fundamental role of SP in the detection of NPs: SP strongly enhances both the evanescent waves scattered from the NPs and the plasmon wave (due to gold roughness), leading to a slow increase in $\Delta I/I_0$ versus the size of the NP. From a technical point of view, the detection of even smaller NPs should be possible with SSPM by modifying the gold film roughness via either a thermal or a chemical treatment of the samples.[16,22] This work demonstrates that SSPM is a very promising nonintrusive optical technique for visualizing soft nanomaterials such as polymers, gels, macromolecular objects, and biological molecular assemblies, with no need of markers (as commonly used in fluorescence microscopy).

ACKNOWLEDGMENTS

We are very grateful to A. Arneodo for a critical reading

of the manuscript. We acknowledge the funding of Région Rhône Alpes under an Emergence project (2005). We are also very endebted to the French Agency for Research (ANR) which funded initially our project under Contract No. ANR-06-PCVI-0026 and to Lyon Science Transfert (Université of Lyon) for his technical and financial support (2008). Computing facilities from IDRIS and pôle M3PEC (Univ. Bordeaux, Région Aquitaine) were used.

[1] H. Raether, *Surface Plasmons on Smooth and Rough Surfaces and on Gratings*, Springer Tracts in Modern Physics Vol. 111 (Springer, Berlin, 1988).
[2] J. Homola, S. Yee, and G. Gauglitz, Sens. Actuators B **54**, 3 (1999).
[3] J. J. Mock, M. Barbic, D. R. Smith, D. A. Schultz, and S. Schultz, J. Chem. Phys. **116**, 6755 (2002).
[4] W. L. Barnes, A. Dereux, and T. W. Ebbesen, Nature (London) **424**, 824 (2003).
[5] M. G. Somekh, S. G. Liu, T. S. Velinov, and C. W. See, Opt. Lett. **25**, 823 (2000).
[6] L. Berguiga, S.-J. Zhang, F. Argoul, and J. Elezgaray, Opt. Lett. **32**, 509 (2007).
[7] H. Kano, S. Mizuguchi, and S. Kawata, J. Opt. Soc. Am. B **15**, 1381 (1998).
[8] A. Bouhelier, F. Ignatovich, A. Bruyant, C. Huang, G. C. des Francs, J.-C. Weeber, A. Dereux, G. Wiederrecht, and L. Novotny, Opt. Lett. **32**, 2535 (2007).
[9] M. El-Sayed, Acc. Chem. Res. **37**, 326 (2004).
[10] G. Wiederrecht, Eur. Phys. J.: Appl. Phys. **28**, 3 (2004).
[11] M. van Dijk, M. Lippitz, and M. Orrit, Acc. Chem. Res. **38**, 594 (2005).
[12] S. Berciaud, D. Lasne, G. A. Blab, L. Cognet, and B. Lounis, Phys. Rev. B **73**, 045424 (2006).
[13] F. V. Ignatovich and L. Novotny, Phys. Rev. Lett. **96**, 013901 (2006).
[14] E. Kretschmann and H. Raether, Z. Naturforsch. A **23**, 2135 (1968).
[15] A. Otto, Z. Phys. **216**, 398 (1968).
[16] S. Zhang, L. Berguiga, J. Elezgaray, T. Roland, C. Faivre-Moskalenko, and F. Argoul, Surf. Sci. **601**, 5445 (2007).
[17] J. Lekner, *Theory of Reflection of Electromagnetic and Particle Waves* (Martinus Nijhoff, Dordrecht, 1987).
[18] E. Kretschmann, Z. Phys. **241**, 313 (1971).
[19] H. Raether, *Excitation of Plasmons and Interband Transitions by Electrons* (Springer-Verlag, Berlin, 1980).
[20] A. Hohenau, J. Krenn, A. Stepanov, A. Drezet, H. Ditlbacher, B. Steinberger, A. Leitner, and F. Ausseneg, Opt. Lett. **30**, 893 (2005).
[21] M. G. Somekh, S. G. Liu, T. S. Velinov, and C. W. See, Appl. Opt. **39**, 6279 (2000).
[22] T. Roland, A. Khalil, A. Tanenbaum, L. Berguiga, P. Delichère, L. Bonneviot, J. Elezgaray, A. Arneodo, and F. Argoul, Surf. Sci. **603**, 3307 (2009).
[23] J. Elezgaray, T. Roland, L. Berguiga, and F. Argoul, J. Opt. Soc. Am. A **27**, 450 (2010).